Effects of annealing temperature on the structure and photoluminescence properties of the ZnO/ZnAl$_2$O$_4$/Ca$_5$Al$_6$O$_{14}$/Ca$_3$Al$_4$ZnO$_{10}$:0.1% Ce^{3+} mixed-phases nanophosphor prepared by citrate sol-gel process

M.N. Mphelane[1], M.R. Mhlongo[1], T.E. Motaung[2], L.F. Koao[3], T.T. Hlatshwayo[4], S.V. Motloung[1,5*]

[1]Department of Physics, Sefako Makgatho Health Science University, Medunsa, 0204, South Africa

[2]Department of Chemistry, University of Zululand, KwaDlangezwa, 3886, South Africa

[3]Department of Physics, University of the Free State (Qwaqwa Campus), Phuthaditjhaba, 9866, South Africa

[4]Physics Department, University of Pretoria, South Africa

[5]Department of Physics, Nelson Mandela University, Port Elizabeth 6031, South Africa

Corresponding author:

E-mail: cchataa@gmail.com (Setumo Victor Motloung)

Abstract.

Mixed-phases of the undoped ZnAl$_2$O$_4$/ZnO/Ca$_5$Al$_6$O$_{14}$ (ZZC) and Ce^{3+} doped ZnAl$_2$O$_4$/ZnO/Ca$_5$Al$_6$O$_{14}$/Ca$_3$Al$_4$ZnO$_{10}$ (ZZCC:0.1% Ce^{3+}) were successfully prepared using the sol-gel method. The 0.1% Ce^{3+} concentration was kept constant while the annealing temperature (T$_a$) was varied from 500 – 1300 ^{o}C. X-ray diffraction (XRD) results showed that the prepared materials consist of the mixture of the cubic (ZnAl$_2$O$_4$), hexagonal wurzite (ZnO) and orthorhombic (Ca$_5$Al$_6$O$_{14}$ and Ca$_3$Al$_4$ZnO$_{10}$) crystal structures, which highly depends on the T$_a$. Energy dispersive x-ray spectroscopy (EDS) analysis confirmed the presence of all the expected elementary compositions. Scanning electron microscopy (SEM) results showed that varying the T$_a$ does not influence the morphology of the prepared nanophosphor material. Transmission Electron Microscopy (TEM) confirmed that the prepared powders were in the nanoscale region. The photoluminescence (PL) results showed emission peaks located at 409, 488, 545, 589, 615, 695 and 785 nm, which were attributed to the intrinsic defects within ZZC mixed phases. There was no emission observed from the Ce^{3+} transition. Optimum photoluminescence intensity was observed at the T$_a$ = 600 °C. The commission Internationale de I'Eclairage coordinates (CIE) showed that the emission colour could be tuned by varying the T$_a$.

Keywords: Sol-gel; Spinel; Ce^{3+}-doped; Luminescence; CIE

1. Introduction

Recently nanoparticles research is currently an area of substantial scientific interest to researchers. In particular, metal oxide nanoparticles have received research attention due to their remarkable optical, electrical, magnetic and catalytic properties [1]. Metal oxide nanoparticles such as zinc oxide (ZnO) with a bandgap of $E_g \sim 3.37$ eV [2], can be used in light-emitting diodes (LEDs), transport electrodes, liquid crystals and solar cells [3, 4]. ZnO has been reported [3 - 5] to emit intrinsic luminescence in the green spectral range and minor emission in the red spectral region. These emissions are due to deep defects such as oxygen and zinc vacancies and impurities. Other metal oxide materials such as zinc aluminate ($ZnAl_2O_4$) which is well known for its wide $E_g \sim 3.8$ eV, has attracted researchers due to its photo-electronic and optical applications. This material can be used as an ultraviolet (UV) transparent conductor, sensors, dielectric material, high temperature ceramic, catalyst, and catalyst support [6]. This material has a close-packed face-centered cubic (FCC) structure with Fd3m space group symmetry. The other oxide material of interest to researchers around the globe is calcium aluminate ($CaAl_2O_4$). This is due to its potential use in a wide range of applications such as optical and structural ceramics, high performance polymer-modified cement-based materials, steel making and refining of steel [7, 8]. There are many other phases of calcium aluminate such as $CaAl_2O_4$ [7], $CaAl_4O_7$ [9], $CaAl_{12}O_{19}$ [10], $Ca_3Al_2O_6$ [11] and $Ca_{12}Al_{14}O_{33}$ [9] which have been reported. In this work, the focus is drawn on the $Ca_5Al_6O_{14}$ and $Ca_3Al_4ZnO_{10}$. $Ca_5Al_6O_{14}$ has an orthorhombic crystal structure with a space group of $Cmc2_1$ and $E_g \sim 4.23$ eV [12, 13], whereas $Ca_3Al_4ZnO_{10}$ is orthorhombic in structure with space group *Pbc21* and lattice constants $a = 5.1420$, $b = 16.7560$ and $c = 10.7100$ Å [14]. Synthesis conditions such as starting materials stoichiometric ratios, concentrations and temperature plays a very important to the formation of the single phase [15]. These oxide materials have been prepared traditionally by solid-state reactions [16], co-precipitation method [17], hydrothermal [18], combustion [7] and sol-gel [6, 16]. Compared with other synthesis methods, sol-gel route is a versatile and attractive technique [6] since it has high homogeneity, good stoichiometric control and produces pure and ultrafine powders [19].

Cerium (Ce^{3+}) ions are attractive trivalent rare-earth ions used in the doping of various host material. Ce^{3+} has broad band emissions consisting of two peaks at 320 and 450 nm which are caused by 5d-4f transitions [20]. Brito et al. [21] studied the effects of Ce^{3+} concentration in $CaAl_2O_4$ prepared by the sol-gel process. The results showed that the emission at 450 nm (blue) was related to the Ce^{3+} ion, while an emission at 650 nm (red) was caused by the intrinsic defects from the host matrix. Up to so far in a literature, there is no study particularly investigating the $Ca_5Al_6O_{14}$:Ce^{3+}. Shukla et al. [22] prepared ZnO nanoparticles doped with Ce^{3+} using the co-precipitation method. The doped samples showed emission peaks at 392, 440, 520 and 550 nm, which were assigned to $^2D_{3/2} \rightarrow {}^2F_{5/2}$, $^2D_{3/2} \rightarrow {}^2F_{7/2}$ and $^5D_0 \rightarrow {}^7F_0$ transitions of Ce^{3+}, respectively. Singh et al. [23] reported the effects of varying Ce^{3+} concentrations in $ZnAl_2O_4$: Ce^{3+}. The PL results revealed a broad emission band at 360 nm, which was assigned to the parity allowed electron $^5D_0 \rightarrow {}^2F_{5/2}$ transitions of Ce^{3+} ions. The primary aim of this study

was to synthesize the $Zn_{0.5}Ca_{0.5}Al_2O_4$:0.1% Ce^{3+} nanoparticles for possible application in light emitting devices. It was anticipated that the material $Zn_{0.5}Ca_{0.5}Al_2O_4$ might possibly have the combined properties of both the bulk $ZnAl_2O_4$ and $CaAl_2O_4$. However, it was interesting to repetitively realize that the results turned-out to constitute of the $ZnO/ZnAl_2O_4/Ca_5Al_6O_{14}/Ca_3Al_4ZnO_{10}$ (hereafter called ZZCC) mixed phases, which are highly relying on the T_a. Therefore, in this study we report on the effect of T_a on the structural and photoluminescence (PL) properties of the ZZCC:0.1% Ce^{3+}. The emissions channels associated with the observed PL emissions are also proposed.

2. Experimental

2.1. Synthesis

The undoped $ZnAl_2O_4$, $Ca_5Al_6O_{14}$, $ZnO/ZnAl_2O_4/Ca_5Al_6O_{14}$ (hereafter called ZZC), ZZCC:0.1% Ce^{3+} nanophosphors were successfully synthesized using citrate sol-gel method. Zinc nitrates hexhydrate $[Zn(NO_3)_2 \cdot 6H_2O, 98 \%]$, calcium nitrates $[Ca(NO_3)_2, 99 \%]$, aluminium nitrates nano-hydrate $[Al(NO_3)_3 \cdot 9H_2O, 98.5 \%]$, citric acid (CA) $[C_6H_8O_7 \cdot H_2O, 99 \%]$ were the starting materials. All of the employed chemicals were purchased from Sigma Aldrich and were used without any further purification. The $ZnAl_2O_4$ was prepared by adding the starting masses of the precursors 4.373 g $(Zn(NO_3)_2 \cdot 6H_2O)$, 10.808 g $(Al(NO_3)_3 \cdot 9H_2O)$ and 2.328 g (CA) in a beaker and were dissolved by adding 30 ml of de-ionized water. The $Ca_5Al_6O_{14}$ was prepared by adding the 3.507 g of $(Ca(NO_3)_2)$ and 10.919 g $Al(NO_3)_3 \cdot 9H_2O$ in a beaker and were dissolved by adding 30 ml of de-ionized water. The ZZC and ZZCC were prepared by adding the 4.373 g $(Zn(NO_3)_2 \cdot 6H_2O)$, 3.507 g $(Ca(NO_3)_2)$, 10.864 g (Al) and 2.328 g (CA) all in one beaker and were dissolved by adding 30 ml of de-ionized water. The doped samples (ZZCC:0.1% Ce^{3+}) was prepared by adding 0.006 g of $[Ce(NO_3)_3 \cdot 4H_2O, 99.9\%]$ to the solution. The heating temperature was kept at ~ 80 ^{o}C for all samples while constantly stirring the solution using a magnetic stirrer. The gels were dried at room temperature for 12 h to allow enough gelling. The resulting dried gels were annealed between 500 − 1300 °C for 1 h in air. The foamy-like products were left to cool off at room temperature then ground and pulverized (reduced to a fine powder). The resulting powders were taken for characterization with various techniques.

2.2. Characterization

Bruker D8-Advance powder XRD with a CuKα (1.5405 Å) radiation and JEOL JEM 1010 transmission electron microscopy (TEM) were used to study the crystal structure and crystallite size of the prepared nano-powders. The phases were identified using X'Pert Highscore plus software. The relative phase amounts (weight %) were estimated using the Rietveld method. Zeiss Supra 55 electron microscope (SEM) coupled with an energy dispersive X-ray spectroscope (EDS) was used to study the surface morphology, the elementary composition and elementary distribution. Photoluminescence spectra and the lifetime measurements were performed at room temperature by the Hitachi F-7000 fluorescence spectrophotometer.

3. Results and discussion

3.1. XRD

Fig. 1 shows XRD patterns of the powder products annealed in air at 800 °C. The results shows that the undoped sample resembles the mixture of the $ZnO/ZnAl_2O_4/Ca_5Al_6O_{14}$ (hereafter-called ZZC) phases. Fig 1 (b) shows the doped ZZC at $T_a = 800$ °C and ZZCC:0.1% Ce^{3+} at $T_a = 1300$ °C with their corresponding ICSD cards. The reader is advised to take note of the differences between the ZZC and ZZCC (see Table 1 for clarity). The XRD patterns are in good agreement with ICSD card no 075633, 76641, 001714 and 050293 which can be indexed to the hexagonal wurtzite ZnO, cubic $ZnAl_2O_4$ and orthorhombic $Ca_5Al_6O_{14}$ and $Ca_3Al_4ZnO_{10}$ phases, respectively.
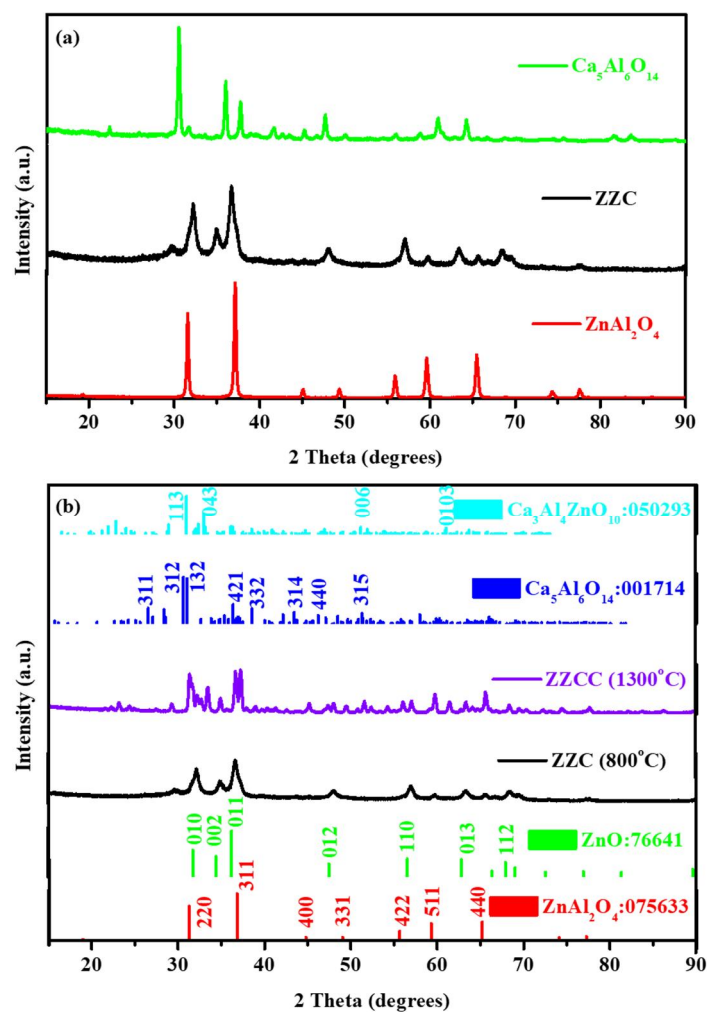

Fig. 1. The XRD patterns for the (a) the undoped (ZZC) (b) ZZC:0.1% Ce^{3+} at 800 °C and ZZCC:0.1% Ce^{3+} at 1300 °C samples and their ICSD standards.

Fig. 2 shows the XRD patterns of the samples annealed at various T_a (500 − 1300 °C). The results suggest that at T_a (500 - 600 °C) the crystallinity of the peaks is poor. Similar crystalline structure

4

was previously observed by Motloung et al. [24] in $ZnO/ZnAl_2O_4$ mixed phases. When comparing the undoped (ZZC) and ZZC:0.1% Ce^{3+} at $T_a = 800$ ^oC, it can be observed that doping with Ce^{3+} does not change the XRD patterns. That is; doping did not change the crystal structure of the ZZC mixed phases and this may be attributed to the low doping concentration of 0.1% Ce^{3+}. Gedekar et al. [11] reported the same behaviour in $Ca_3Al_2O_6$:x% Ce^{3+} prepared by combustion method. At the higher $T_a > 800$ ^oC, the results clearly shows the additional diffraction peaks due to $Ca_3Al_6ZnO_{10}$ suggesting the structural alteration, which could be attributed to the higher T_a.
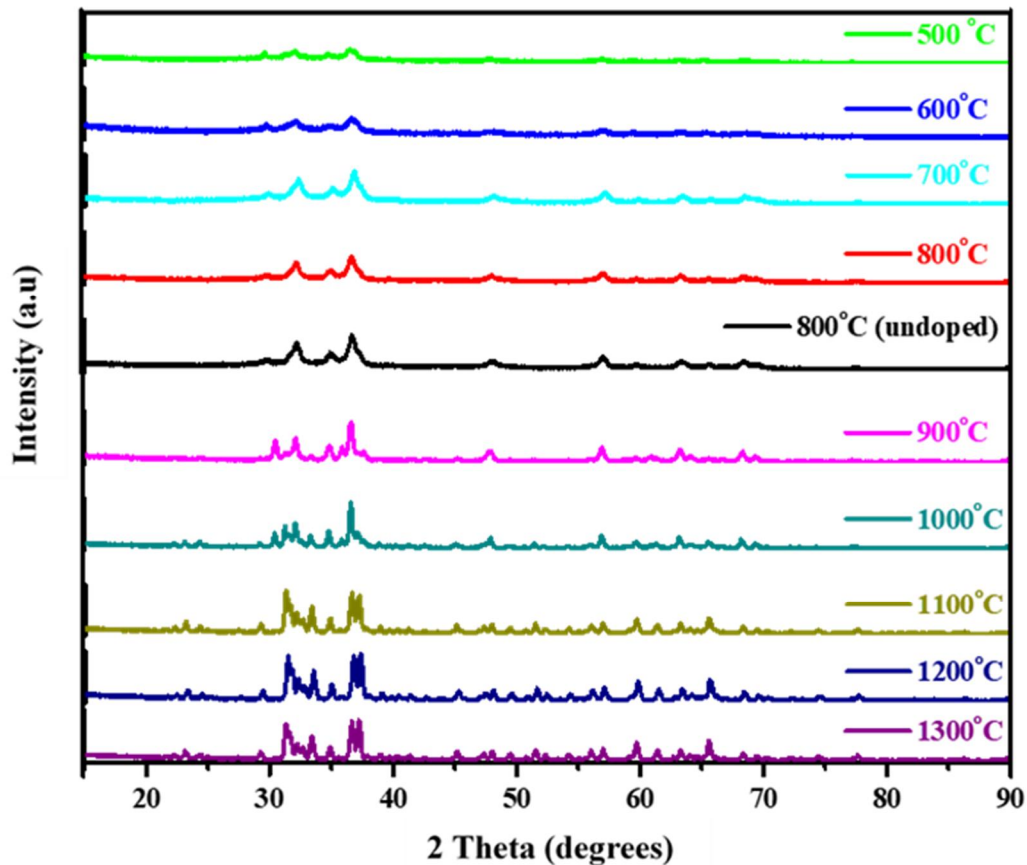

Fig. 2. XRD patterns of the undoped (ZZC) and ZZCC:0.1% Ce^{3+} powders annealed at various T_a.

Table 1 presents the phase quantification (%) in details. In order to deal with the phase quantification precisely, the phase quantification as a function of T_a is shown in Fig. 3. The results reveals that at T_a (500 – 800 ^oC) ZnO is the dominant phase while $ZnAl_2O_4$ and $Ca_5Al_6O_{14}$ phases declines. There is no $Ca_3Al_6ZnO_{10}$ phase at $T_a \leq 800$ ^oC. At $T_a \geq 900$ ^oC $ZnAl_2O_4$ and $Ca_3Al_6ZnO_{10}$ become more pronounced while ZnO and $Ca_5Al_6O_{14}$ phases decreases. This phase dependence on the T_a is certainly anticipated to influence the luminescence, which will be discussed in section 3.5.

Table 1. Phases quantification at various T_a.

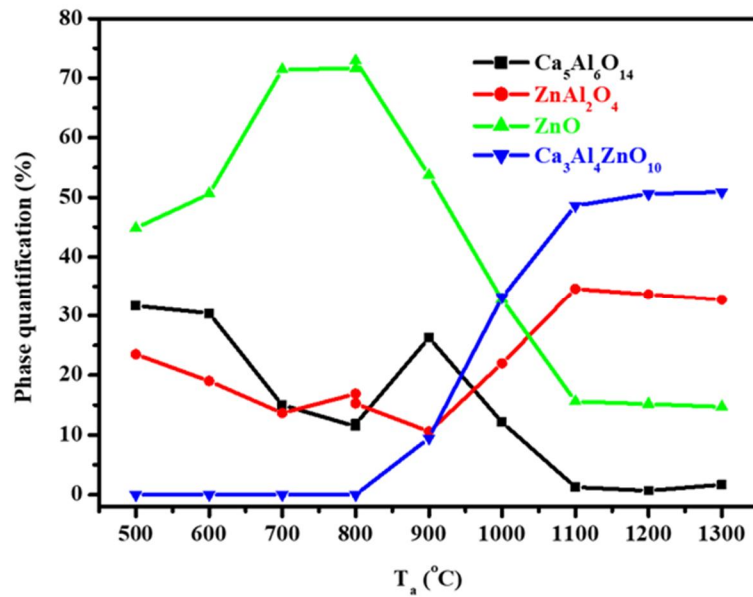| T_a (°C)	ZnO (%)	$ZnAl_2O_4$ (%)	$Ca_5Al_6O_{14}$ (%)	$Ca_3Al_4ZnO_{10}$ (%)
500	44.82	23.49	31.69	0
600	50.6	19.02	30.38	0
700	71.42	13.63	14.96	0
800*	71.65	16.88	11.47	0
800	72.89	15.26	11.85	0
900	53.69	10.58	26.26	9.47
1000	32.77	21.98	12.12	33.13
1100	15.58	34.59	1.24	48.59
1200	15.15	33.64	0.64	50.57
1300	14.71	32.74	1.65	50.89

*Undoped sample

Fig 3. Phase quantification as a function of T_a.

The average crystallite size of the prepared samples was estimated using Scherrer's [23] equation (1)

$$D = \frac{0.9\lambda}{\beta cos\theta} \tag{1}$$

where D is the crystallite size (nm), λ is the radiation wavelength (0.15406 nm), β is the full width at half maximum (FHWM) in radians and θ is the angle of the diffraction (in degree). The diffraction peaks (011), (311), (132) and (113) were used to estimate the crystallite sizes for the ZnO, $ZnAl_2O_4$,

$Ca_5Al_6O_{14}$ and $Ca_3Al_4ZnO_{10}$, respectively. In order to distinguish the diffraction peaks of (ZnO and $ZnAl_2O_4$) and ($Ca_5Al_6O_{14}$ and $Ca_3Al_4ZnO_{10}$) from each order, the deconvolution of peaks 011 and 311 method, which was previously used in [25] were performed in this study. Table 2 presents the estimated crystallite sizes for the samples prepared at various T_a. Fig. 4 shows the crystallite sizes as a function of T_a. Fig. 4 (a) shows that the crystallite sizes fluctuates with an increase in T_a. However, the crystallites sizes for the ZnO, $Ca_5Al_6O_{14}$ and $Ca_3Al_4ZnO_{10}$ increases with an increasing in T_a up-to a certain T_a then decreases as shown in Fig. 4 (a) and (b). The increase in crystallite sizes with increasing T_a is due to the merging process induced by thermal annealing. During annealing or heating process when particles are formed, they collide and either coalesce with one another to form larger particles [26]. Yang et al. [27] suggested that the merging process to form larger ZnO grains as T_a was increased is favoured by the dangling bonds of zinc and oxygen defects at the grain boundaries.

Table 2. Crystallite sizes of different phases at various T_a.

	Crystallite sizes (nm)			
T_a (ºC)	011 of ZnO	311 of $ZnAl_2O_4$	132 of $Ca_5Al_6O_{14}$	113 of $Ca_3Al_4ZnO_{10}$
500	8	8	10	-
600	8	8	9	-
700	13	37	12	-
800*	13	29	13	-
800	14	31	13	-
900	25	10	30	6
1000	37	9	36	25
1100	28	31	29	35
1200	27	32	30	37
1300	27	33	30	29
$ZnAl_2O_4$	-	29	-	-
$Ca_5Al_6O_{14}$	-	-	13	-

*Undoped sample
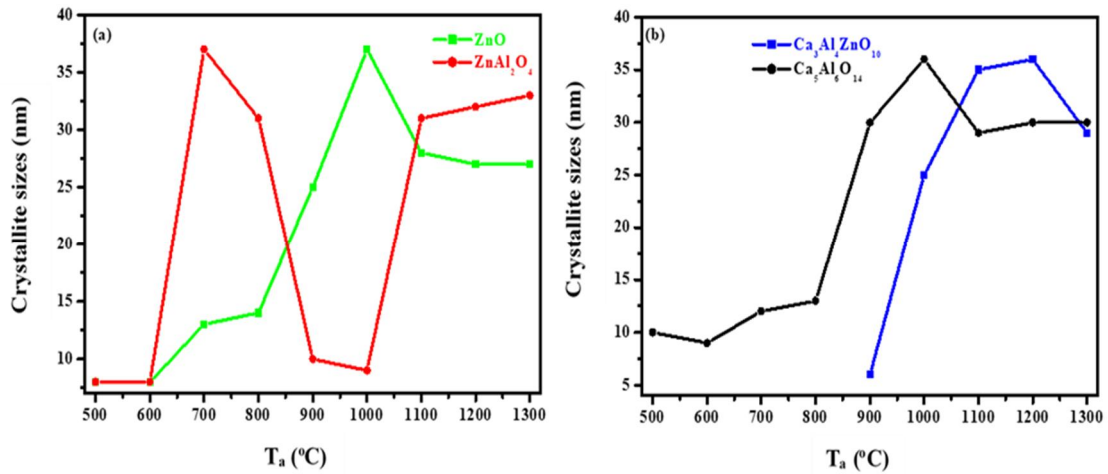
Fig. 4. Crystallite sizes as a function of the T_a for the (a) 011 ZnO and 311 $ZnAl_2O_4$ (b) 132 $Ca_5Al_6O_{14}$ and 113 $Ca_3Al_4ZnO_{10}$ phases.

3.2. EDS

The undoped ZZC at Ta = 800 ^{o}C nanophosphor material was further analysed by EDS mapping and the images are presented in Fig 5. The EDS mapping was employed to confirm the elemental distribution of Zn, Ca, Al and O elements present in the sample. The images clearly indicate that the elements are distributed all over the surface on the surface of the prepared sample.
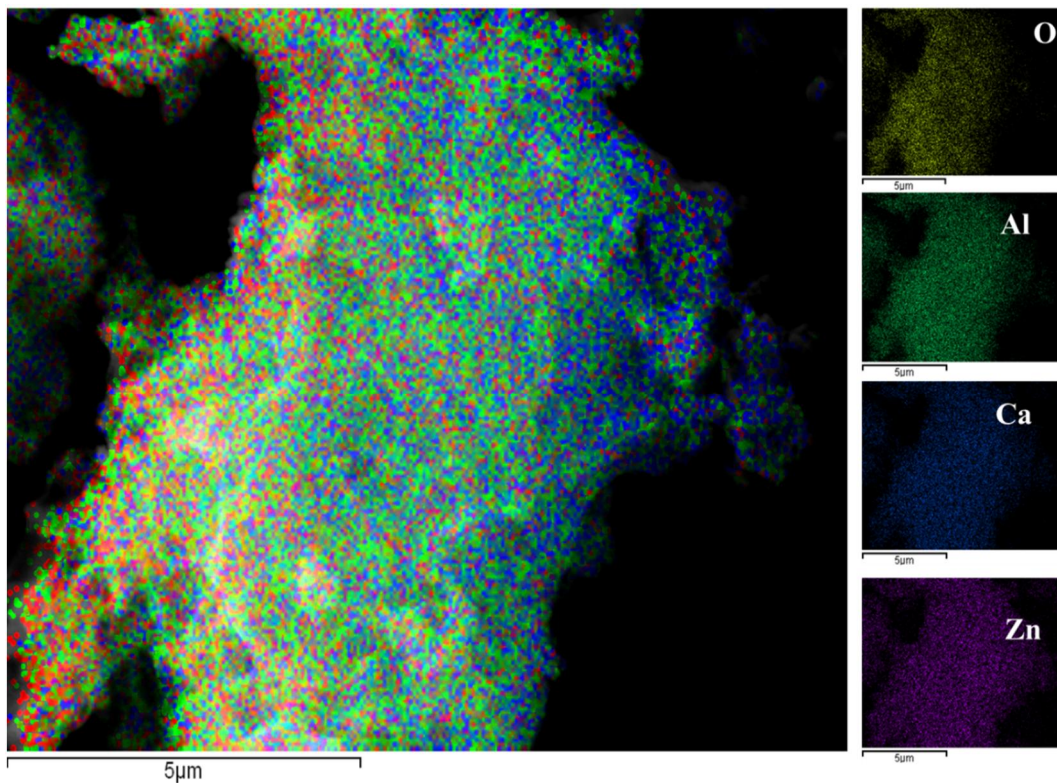

Fig. 5. EDS mapping of the undoped ZZC at T_a (800 ^{o}C) sample.

8

3.3. SEM

The morphological aspects of the selected prepared samples. The micrographs consist of irregular particles distributed randomly on the surface of the prepared samples. ZZCC:0.1% Ce^{3+} annealed at 500 and 600 °C (as shown in Fig 6 (a) and (b), respectively), shows that the particles are distributed on a smooth surface and there pores present. While Fig 6 (c), (d) and (e) show that the particles are distributed on a rough surface. These results suggest that varying T_a does not significantly influence the morphology of the prepared nanophosphors.
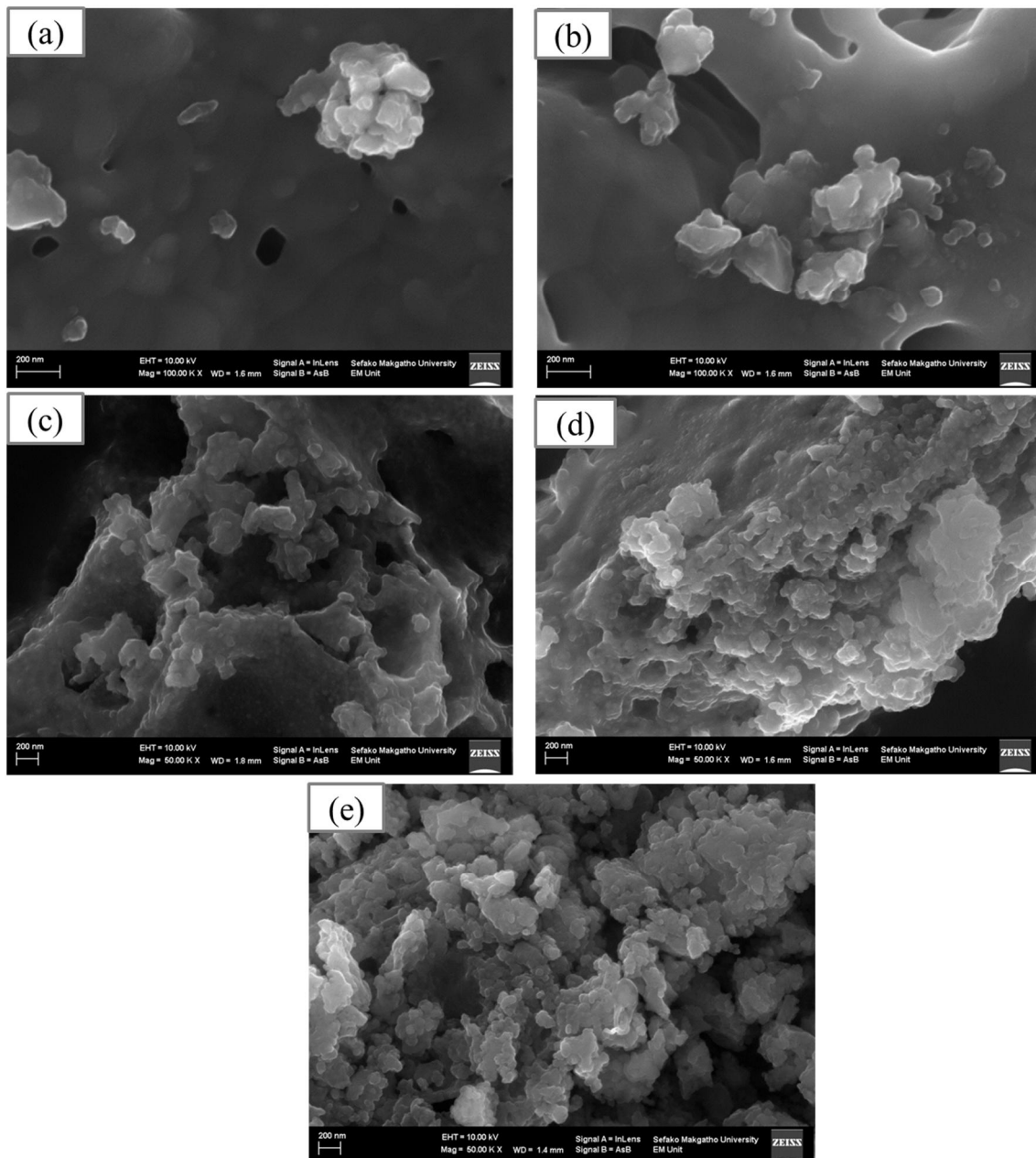

Fig. 6. SEM micrographs of the prepred nanopowders at T_a of (a) 500 (b) 600 (c) 800 (undoped ZZC) (d) 800 and (e) 1300 °C.

3.4. TEM

The prepared nano-phosphor samples for the ZZCC undoped and ZZCC:0.1% Ce^{3+} annealed at 800 °C were further examined by the TEM as shown in Fig 7 (a) and (b), respectively. Both micrographs show agglomeration of irregular crystallites, hence it is a hard task to estimate the particle sizes.
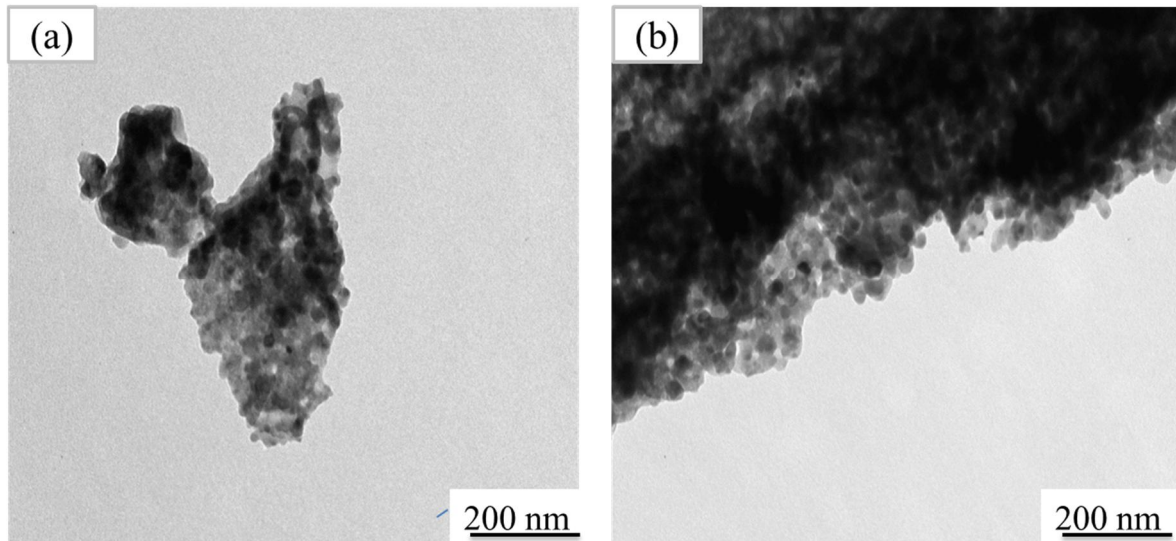

Fig. 7. TEM micrographs of the (a) ZZC (undoped) and (b) ZZC:0.1% Ce^{3+} samples.

3.5. PL

The excitation and emission spectra of the undoped $Ca_5Al_6O_{14}$ and $ZnAl_2O_4$ at $T_a = 800$ °C is shown in Fig. 8 (a). The excitation spectra were recorded when monitoring the emission at 409 nm and there are three excitation peaks at 277, 314 and 383 nm. Considering the range of bandgap energy of $ZnAl_2O_4$ to be 4.46 - 5.71 eV [28], the broad excitation peaks at 277 nm (~ 4.48 eV) can be attributed to band-to-band transition $ZnAl_2O_4$ [29, 21]. The excitation peak at 314 nm (~ 3.95 eV) and 383 nm (~3.24 eV) may be due to the intrinsic defects within both the $ZnAl_2O_4$ and ZnO [24, 30]. Motloung et al. [24] reported an absorption band at 330 nm which was attributed to the defects levels of the $ZnAl_2O_4$ nanomaterial. On the other hand, Pushpa et al. [30] reported an excitation peak at 325 nm and was attributed to intrinsic defects in the ZnO. The emission spectra show one broad emission band located at 409 nm (~ 3.03 eV) when monitoring the excitation at 277 nm. The emission peak at 409 can be assigned to the intra-bandgap defects of the $ZnAl_2O_4$ and ZnO [31, 32]. Wang et al. [31] reported two emission peaks located at 400 and 410 nm in $ZnAl_2O_4$ and they were attributed to the oxygen vacancies. Garces et al. [32] reported the emission band at 409 nm in ZnO: Cu which was due to oxygen/zinc vacancy. The normalized emission spectra of the $ZnAl_2O_4$ and $Ca_5Al_6O_{14}$ is shown in Fig. 8 (b). The spectra show that there are seven emission bands at 409, 488, 545, 589, 615, 694 and 785 nm. The emission peak at 488 nm corresponds to the radiative transition of an electron from interstitial Zn (Zn_i) level to the top of valence band (VB) in $ZnAl_2O_4$ and ZnO [30, 33]. Pushpa et al. [30] on the investigation of red luminescence from ZnO: Cr^{3+} under visible excitation showed an emission at 484

nm related to electrons in the acceptor level (*Vzn*). Similar results reported by Cheng et al. [33] suggested that the blue-green emission at 488 nm was coming from defects such as zinc vacancies within the ZnAl$_2$O$_4$ crystals. The green emission peak at 545 nm was previously reported to originate from electron-hole recombination taking place at the defect sites of the ZnO material i.e. the oxygen vacancy [3]. Silva et al. [34] reported a similar emission band at 545 nm, which was attributed to the defects from oxygen vacancies in ZnAl$_2$O$_4$. This results suggest that the emission at 545 nm can be attributed to both the ZnO and ZnAl$_2$O$_4$. The green-yellow emission band located at 589 nm and orange-red emission 615 nm are attributed to the band transition from the interstitial zinc (*Zn$_i$*) to the interstitial oxygen (*O$_i$*) defects sites in ZnO [35, 36, 37]. The radiative electrons which are deeply trapped by the holes can be located at 2.11 eV (589 nm) and 2.02 eV (615 nm) below the CB of the ZnO nanomaterial. The emission band at 694 and 785 nm is attributed to excess/ surplus of oxygen impurities within ZnO crystals [2, 3, 38 ,39]. The electron traps at 1.79 eV (694 nm) and 1.58 eV (785 nm) below the CB results in the red luminescence.
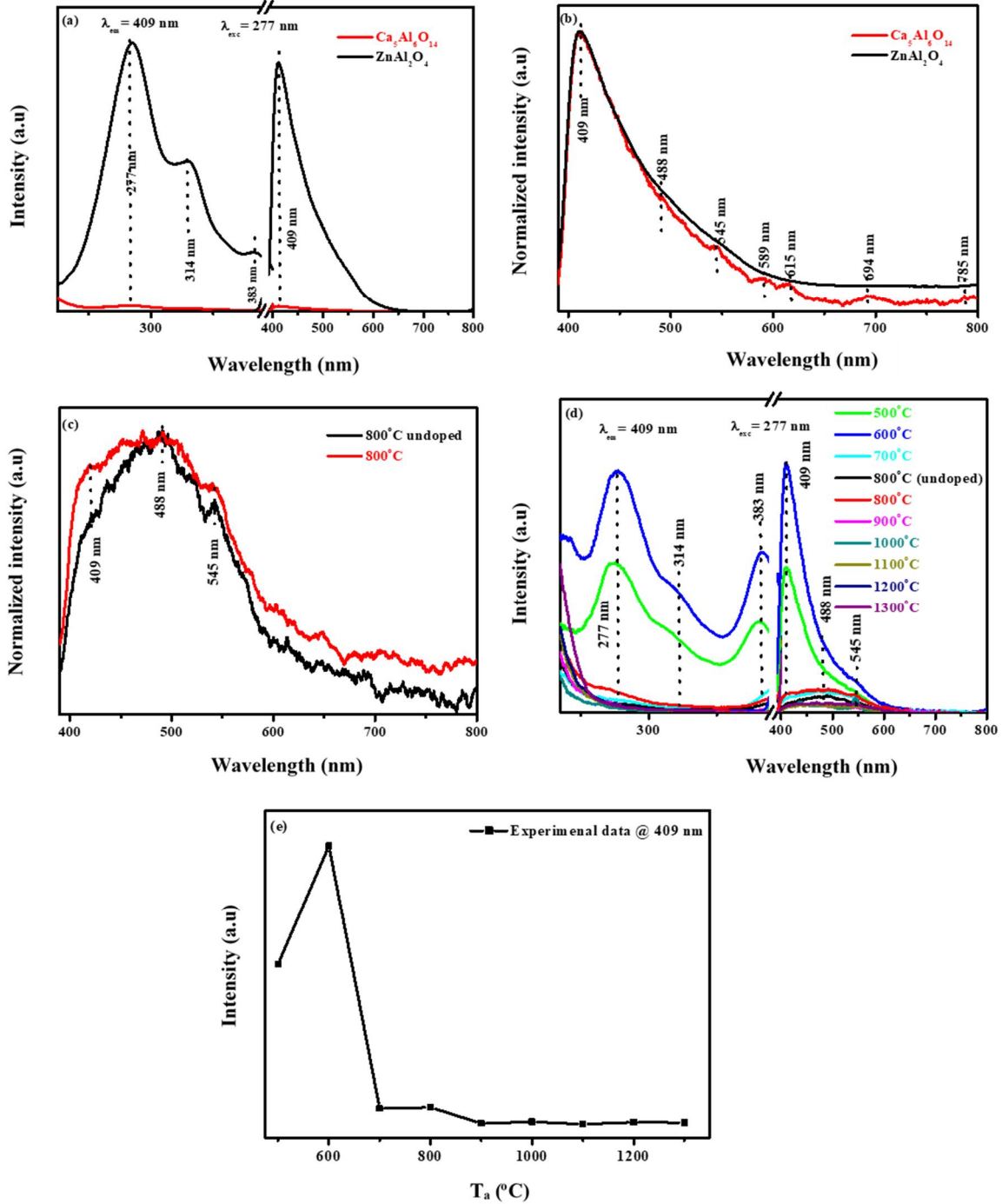
Fig. 8. (a) Excitation and emission spectra of the $Ca_5Al_6O_{14}$ and $ZnAl_2O_4$ (b) normalized emission spectra of $Ca_5Al_6O_{14}$ and $ZnAl_2O_4$ (c) normalized emission intensity as a function of wavelength for the undoped and ZZC:0.1% Ce^{3+} annealed at 800 °C (d) excitation and emission spectra of the prepared nanophosphor series and (e) emission intensity as a function of T_a of the ZZCC:0.1% Ce^{3+}.

The normalized emission intensity of the ZZC and ZZC:0.1% Ce^{3+} samples at T_a = 800 °C is shown in Fig. 8 (c). It is clear that there was no emission from the Ce^{3+} transition as all observed emissions therein are attributed to originate from the same notion as discussed in Fig. 8 (a) and (b). The

excitation and emission spectrum of the prepared nanophosphor samples at various T_a is shown in Fig. 8 (d). For the samples annealed at 800 °C, it is clear that doping enhances the luminescence intensity of the undoped ZZC. All of the excitation and emissions observed are attributed to arise from the same notion as described in Fig. 8 (a) and (b). At the low T_a = 500 and 600 °C, it can be noted that there are two emission bands at around 409 and 545 nm. At the higher T_a = 700 - 1300 °C, it can be observed that there is an emergence of a broad band peak with maximum around 488 nm. It is reasonable to propose that this new peak might be due to both the ZnO and $ZnAl_2O_4$. Even though there is an additional $Ca_3Al_4ZnO_{10}$ phase emerging at T_a = 900 °C, there is no evidence of an emission which could be attributed to this phase. This is supported by the fact that Cao et al. [40] did not observe any emission from $Ca_3Al_4ZnO_{10}$ (host) in the $Ca_3Al_4ZnO_{10}$:Mn^{4+} system. The deep red emission was attributed to Mn^{4+}. Fig. 8 (e) shows the 409 nm emission intensity as a function of T_a and the results suggest that the 600 °C is an optimum T_a. The increase in emission intensity is due to the luminescence enhancement [41], while the decrease is due to luminescence quenching [42]. As it was anticipated on the XRD results in Fig. 3 that the phase dependence on the T_a will influence the PL emission, the results suggest that the observed intense emission shown in Fig. 8 (d) and (e) at the lower T_a is mostly contributed by the ZnO phase. As the T_a increases, the ZnO phase content decreases which is accompanied by the decrease in PL emission intensity. The main reason for the luminescence quenching at higher T_a might possibly be due to the gradually reacting of ZnO phase with Al_2O_3 or CaO and $Ca_5Al_6O_{14}$ facilitated by higher T_a to formed non-radiative $Ca_3Al_4ZnO_{10}$ phase as the ZnO phase is decreasing (see Fig. 3). The proposed excitation and emission pathway mechanism are presented in Fig. 9.
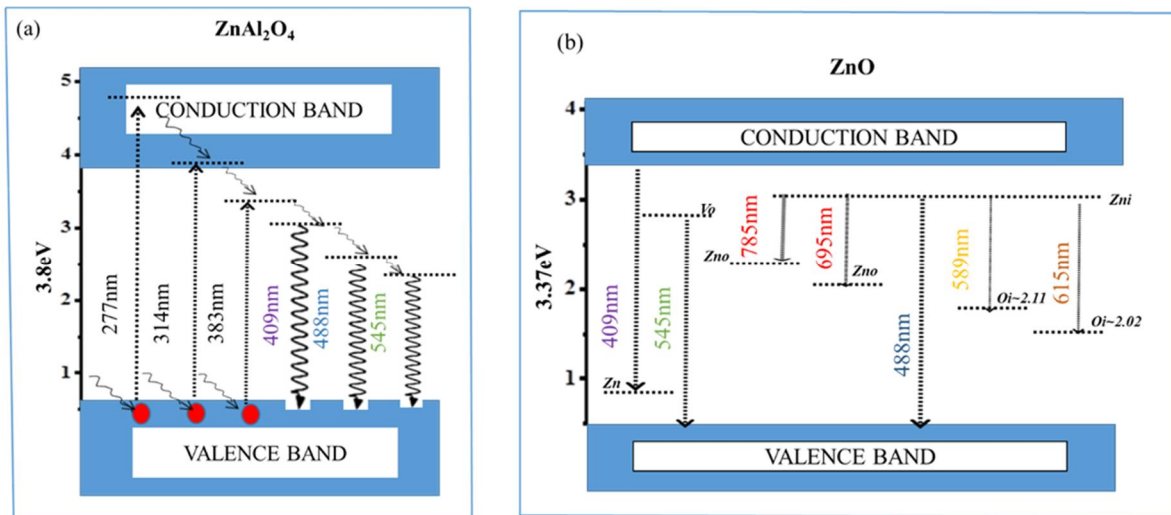

Fig. 9. The proposed excitation and emission pathway mechanism in (a) $ZnAl_2O_4$ and (b) ZnO.

Studies on the phosphorescence decay time on the prepared samples are presented in Fig. 10. The phosphorescence decay time was taken under the 277 nm excitation and 409 nm emission

wavelength. The results show that all the prepared nanophosphor samples have the same afterglow mechanism. All the decay curves were fitted better using the first order decay shown in equation 2

$$I(t) = Ae^{\frac{-t}{\tau}} + y_0 \tag{2}$$

where I represent the phosphorescent intensity, A is a constant which contribute to the fast decay component, t (ms) is the time of measurement, τ (ms) is the fast time value and y_0 is the initial luminescence intensity values which are presented in Table 3.
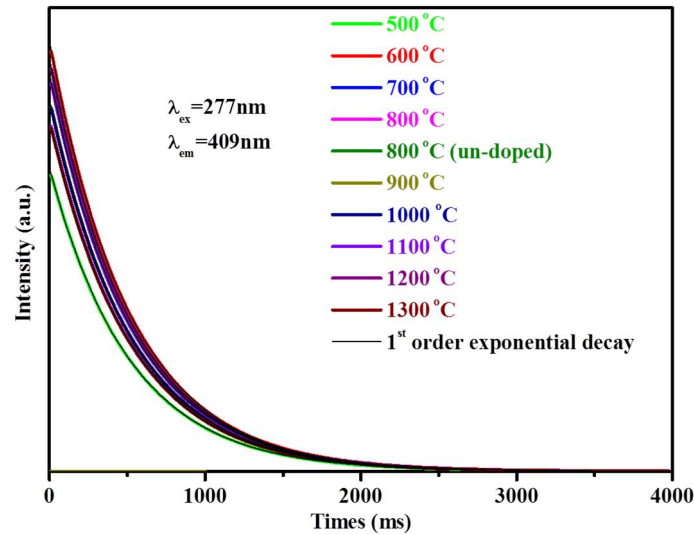

Fig. 10. The decay curves of the prepared series at various T_a.

Table 3: Summary of the sample identification, lifetime measurements and CIE coordinates.

T_a (°C)	y_0	A	τ (ms)	CIE Coordinates (x;y)
500	0.286	980	514.76	(0.1727;0.1459)
600	0.319	1390	514.15	(0.1780;0.1397)
700	0.320	1332	513.62	(0.2121;0.3009)
800*	0.382	1204	513.61	(0.1816;0.2896)
800	0.349	1142	513.73	(0.2136;0.2911)
900	0.100	1147	513.62	(0.1789;0.2830)
1000	0.680	1199	513.67	(0.2162;0.3022)
1100	0.397	1283	513.69	(0.1794;0.2854)
1200	0.177	1333	513.64	(0.2137;0.3117)
1300	0.130	1134	513.67	(0.1328;0.2516)
$ZnAl_2O_4$	1.203	5758	517.55	(0.1738;0.1609)
$Ca_5Al_6O_{14}$	0.886	1537	513.90	(0.1764;0.1541)

* Undoped sample

The CIE colour coordinates measured from PL emission of the undoped and ZZC:0.1% Ce^{3+} nanoparticles annealed at various T_a (500 – 1300 °C) are shown in Fig. 11. The chromaticity coordinates (x;y) of the prepared phosphors were estimated as shown in Table 3. Fig. 11 (a) shows the CIE diagram of the undoped, $ZnAl_2O_4$ and $Ca_5Al_6O_{14}$, which suggest that these materials can produce a blue light. The CIE diagram of the ZZCC:0.1% Ce^{3+} prepared samples at various T_a is shown in Fig. 11 (b). The results show that as the T_a is increasing the emission colour can be tuned from violet-bluish to greenish.
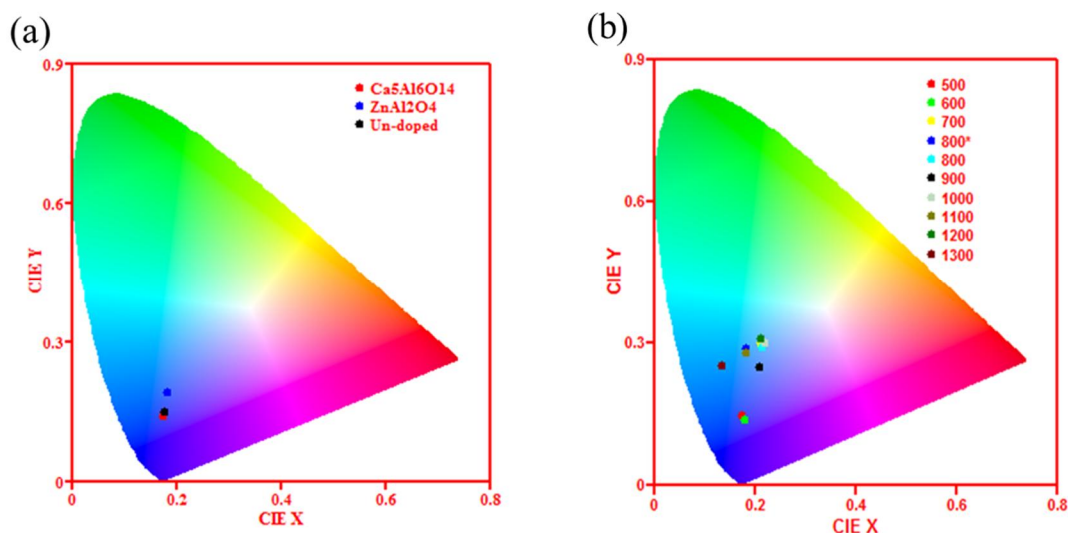

Fig. 11. CIE diagram of the (a) undoped and (b) 0.1% Ce^{3+} doped samples at various T_a (the * denotes the undoped sample).

4. Conclusion

Undoped $ZnAl_2O_4$, $Ca_5Al_6O_{14}$, ZZC and ZZCC:0.1% Ce^{3+} were successfully synthesized by the citrate sol-gel technique. The effect of T_a (500 – 1300 °C) on the properties of the phosphor were studied. The XRD results showed that the phase presence highly depends on the T_a and the $Ca_3Al_4ZnO_{10}$ phase starts to forms at least at 900 °C. Varying T_a influences the crystallite size and peak intensity of the phases present in a prepared phosphor. The PL results showed that ZZC and ZZCC:0.1% Ce^{3+} revealed seven luminescent peaks located at 409, 488, 545, 585, 615, 689 and 785 nm which were attributed to defects states within the ZnO and $ZnAl_2O_4$ nanostructures. The increase in T_a decreased the luminescence intensity, which was due to the decrease in ZnO phase. There was no evidence of an emission from Ce^{3+} transitions. The Commission Internationale de l'Eclairage (CIE) showed that the colour can be tuned from violet to blue and finally to green when varying the T_a.

Acknowledgements

References

[1] N.H.A. Nguyen, V.T.P Vinod, I. Vera, Č. Miroslav, Š. Alena, Nanoscale Res. Lett. 13 (2018) 159.

[2] C. Klingshirn, Phys. Status Solidi B 244 (9) (2007) 3027-3073.

[3] A.S. Kuznetsov, Y.G. Lu, S. Turner, M.V. Shestakov, V.K. Tikhomirov, D. Kirilenko, J. Verbeeck, A.N. Baranov, V.V. Moshchalkov, Opt. Mater. Express 2 (6) (2012) 723-734.

[4] U. Ozgur, D. Hofstetter, H. Morkoc, Proc. IEEE 98 (7) (2010) 1255-1268.

[5] L. Lu, R. Li, K. Fan, T. Peng, J. Sol. Energy 84 (5) (2010) 844-853.

[6] E. Muhammad, A. Jamal, K.D. Sakthi, M.R. Anantharaman, Bull. Mater. Sci. 34 (2) (2011) 251-259.

[7] F.B. Dejene, D.B. Bem, H.C. Swart, J. rare earths 28 (2010) 272-276.

[8] A. Gaki, T-h. Perraki, G. Kakali, J. Europ. Ceram. Soc. 27 (2-3) (2007) 1785-1789.

[9] J.M. Rivas Mercury, A.H. De Aza, P. Pena, J. Europ. Ceram. Soc. 25 (14) (2005) 3269-3279.

[10] P. Li, M. Peng, X. Yin, Z. Ma, G. Dong, Q. Zhang, J. Qiu, Optics Express 21 (16) (2013) 18943-18948.

[11] K.A. Gedekar, S.P. Wankhede, S.V. Moharil, R.M. Belekar, J. Mater. Sci.: Mater. Electro. 29 (8) (2018) 6260-6265.

[12] S.K. Misra, S.I. Andronenko, J. Phys. Chem. of Solids 61 (12) (2000) 1913-1917.

[13] M.G. Vincent, J.W. Jeffery, Acta Cryst. Section B: Structural Crystallography and Crystal Chemistry 34 (5) (1978) 1422-1428.

[14] V.D. Barbanyagre, T.I. Timoshenko, A.M. IIyinets, Shamshurov, Powder Diffraction, 12 (1997) 22

[15] A.H. Wako, PhD Thesis, University of the Free State Republic of South Africa, (2011).

[16] J.T. Keller, D.K. Agrawal, H.A. McKinstry, J. Amer. Ceram. Soc. 3 (4) (1988) 420-422.

[17] K. Petcharoen, A. Sirivat, Mater. Sci. Eng: B 177 (5) (2012) 421-427.

[18] Z. Chen, E. Shi, Y. Zheng, W. Li, N. Wu, W. Zhong, Mater. Lett. 56 (4), (2002) 601-605.

[19] M.T. Tsai, Y.X. Chen, P.J. Tsai, Y.K. Wang, Thin. Sol. Fil. 518 (2010) 5363-5367.

[20] R.J. Wiglusz, T. Grzyb, A. Lukowiak, A. Bednarkiewicz, S. Lis, W. Strek, J. Lumin. 133 (2013) 102-109.

[21] V.R.S. Brito, R.J. dos Santos, P.N.M. dos Anjos, Conf. Proc. (2016).

[22] S.K. Shukla, E.S. Agorku, H. Mittal, A.K. Mishra, Chem. Pap. 68 (2) (2014) 217-222.

[23] V. Singh, N. Singh, M.S. Pathak, V. Dubey, P.K. Singh, Optik 155 (2018) 285-291.

[24] S. V. Motloung, P. Kumari, L. F. Koao, T. E. Motaung, T. T. Hlatshwayo, M. J. Mochane, Mater. Today Commun. 14 (2018) 294-301.

[25] S.V. Motloung, F.B. Dejene, H.C. Swart, O.M. Ntwaeaborwa, J. Lumin. 163 (2015) 8-16.

[26] M. Jyoti, D. Vijay, S. Radha, Int. J. Sci. Res. 3 (11) (2013) 2250-3153.

[27] S. Yang, Y. Liu, Y. Zhang, D. Mo, Bull. Mater. Sci. 33 (3) (2010) 209-214.

[28] T. Hussain, M. Junaid, S. Atiq, S.K. Abbas, S.M. Ramay, B.F. Alrayes, S. Naseem, J. Alloys Compd. 754 (2017) 940-950.

[29] S.V. Motloung, M. Tsega, F.B. Dejene, H.C. Swart, O.M. Ntwaeaborwa, L.F. Koao, T.E. Motaung, M.J. Hato, J. Alloys Compd. 677 (2016) 72-79.

[30] N. Pushpa, M.K. Kokila, B.M. Nagabhushana, H. Nagabhushana, A.J. Reddy, Bull. Mater. Sci. 38 (5) (2015) 1359-1365.

[31] S.F. Wang, G.Z. Sun, L.M. Fang, L. Lei, X. Xiang, X.T. Zu, Sci. Rep. 5 (2015) 12849.

[32] N.Y. Garces, L. Wang, L. Bai, N.C. Giles, L.E. Hallibutton, G. Cantwell, App. Phy. Lett. 81 (2002) 622-624.

[33] B. Cheng, S. Qu, H. Zhou, Z. Wang, J. Nanotechnol. 17 (12) (2006) 2982.

[34] A.A. Da Silva, A. Goncalves, M.R. Davolos, J. Sol-Gel Sci. Technol. 49 (2009) 101-105.

[35] W.M. Jadwisienczak, H.J. Lozykowski, A. Xu, B. Patel, J. Electro. Mater. 31 (7) (2002) 776-784.

[36] N.H. Alvi, K. Ul Hasan, O. Nur, M. Willander, Nanoscale Res. Lett. 6 (1) (2011)130.

[37] E. Musavi, M. Khanlary, Z. Khakpour, J. Lumin. 216 (2019) 116696.

[38] V.V. Osiko, Opt. Spectrosc 7 (6) (1959) 770-775.

[39] Y.M. Gerbshtein, Y.M. Zelikin, Opt. Spectrosc 28 (1970) 521-522.

[40] R. Cao, J. Zhang, W. Wang, T. Chen, Q. Gou, Y. Wen, F. Xiao, Z. Luo, Opt. Mat. 66 (2017) 293-296.

[41] S.V. Motloung, F.B. Dejene, H.C. Swart, O.M. Ntwaeaborwa, J. Sol-Gel Sci. Technol. 70 (3) (2014) 422-427.

[42] H. Tang, H. Berger, P.E. Schmid, F. Levy, G. Burri, Solid State Commun. 87 (9) (1993) 847-850.